Controlling melt flow by nanoparticles to eliminate surface wave induced surface fluctuation

Minglei Qu[a, b], Qilin Guo[a, b], Luis I. Escano[a], Jiandong Yuan[a, b], S. Mohammad H. Hojjatzadeh[a, b], Samuel J. Clark[c], Kamel Fezzaa[c], Tao Sun[c, 1], Lianyi Chen[a, b, *]

[a] Department of Mechanical Engineering, University of Wisconsin-Madison, Madison, Wisconsin 53706, USA

[b] Department of Materials Science and Engineering, University of Wisconsin-Madison, Madison, Wisconsin 53706, USA

[c] X-ray Science Division, Argonne National Laboratory, Lemont, Illinois 60439, USA

* Corresponding author: lianyi.chen@wisc.edu

Corresponding author address: Department of Mechanical Engineering, University of Wisconsin-Madison, Madison, Wisconsin 53706, USA

[1]Current address: Department of Materials Science and Engineering, University of Virginia, Charlottesville, VA 22904, USA.

Abstract

The high surface roughness is one of the major challenges encountered in laser metal additive manufacturing (AM) processes, which is closely related to the melt flow behavior. However, how to control the melt flow in laser metal AM processes to improve surface finish is unknown. Here we reveal the effects of nanoparticles on melt flow behavior at every location of melt pool during laser metal AM process for the first time using Al6061 + TiC nanoparticles system and achieve significant improvement of surface finish by using TiC nanoparticles to control the melt flow and damp the surface wave. Based on the in-situ x-ray imaging observation, the surface wave is fully damped after adding TiC nanoparticles, compared with only 56% damping without nanoparticles during LPBF of Al6061. Our in-depth in-situ x-ray imaging analysis and viscosity measurement

enable us to identify that nanoparticle-induced increase of viscosity causes the fully damping of the surface wave by (1) increasing the internal fluid friction for more efficient wave amplitude reduction, (2) controlling the melt flow to increase the surface wave number, (3) controlling the melt flow to increase the wave damping time. Furthermore, we also quantified the relative contributions of increasing fluid friction, increasing wave number, and increasing damping time to wave damping, which account for 61%, 25%, and 14%, respectively. Our research provides the mechanisms and potential method to address the surface finish challenge in laser metal AM processes.

Keywords:

Nanoparticle, melt flow, additive manufacturing, surface roughness, synchrotron x-ray imaging

1. Introduction

Laser metal AM enables a one-step production of complex parts directly from digital design models [1], potentially revolutionizing the aerospace, biomedical, and automobile industries [2]. However, the rough printed surface is a major challenge encountered during the laser metal AM process, which will adversely affect the mechanical property, such as tensile properties [3], fatigue life [4,5], which limits the final product application. Surface wave (surface rippling) is one of the key contributors to the surface roughness [6,7] and can be dominant under certain laser processing condition [8]. The surface wave originates from the periodic adjustment/fluctuation of vapor depression (also known as depression zone or keyhole) shape mainly due to the dynamic balance of recoil pressure and surface tension pressure, which results in the repeated liquid pushing near the vapor depression rim to generate surface wave [9]. The generated surface wave usually flows

backward (i.e., opposite to the laser scanning direction) along the melt pool surface via Marangoni flow, introducing the surface fluctuation as it solidifies on the as-printed surface [10].

Many post-processing methods have been reported to reduce surface roughness, including chemical-based polishing [11], abrasive flow machining [12], hydrodynamic cavitation abrasive finishing process [13]. However, post processing introduces extra step, cost, and time, which compromises AM process advantages of minimized processing steps and short lead time. Moreover, while post processing techniques can improve the finial printed surface, they cannot address the surface roughness of intermediate layers during printing, which often introduces defects, such as lack of fusion porosity [14]. Therefore, improving the surface finish by solving the intrinsic surface wave problem during laser melting process is important.

The generation and propagation of surface waves are closely related to the melt flow behavior. However, there is no insightful study on the correlation between melt flow and surface wave since it is very difficult to visualize and control the melt flow inside the melt pool.

It was proposed that adding ceramic nanoparticles may alter the melt flow behavior during laser metal AM or laser welding. However, the conclusions reported in previously published papers based on simulation results or theoretical analysis are controversial. For example, adding nanoparticle enhances [15] or diminishes [16] the liquid flow, maintains [17] or reverses [18] the flow direction. Recently, we reported the direct observation of effects of nanoparticles on spatter dynamics, vapor depression fluctuation [19] and keyhole pore formation [20] during laser AM process by x-ray imaging. Yet, how nanoparticles influence melt flow dynamics during laser melting has not been experimentally characterized and is still unclear.

Surface finish improvement by adding microparticles/nanoparticles during laser processing (laser AM and laser polishing) was reported in previous publications, most of which were

attributed to the increase of the absorptivity. For example, adding TiC [15], graphite [21], or SiC [22] particles into Al or Fe can significantly increase the absorptivity, resulting in more sufficient melting to improve the surface finish. In previous study, TiC nanoparticles were also used to eliminate large spatters to improve the surface finish during laser AM of Al6061 [19]. In laser polishing, it was reported that adding Al_2O_3 nanoparticles into Ni can improve the surface finish by reducing the thermocapillary flow induced liquid accumulation at the melt pool tail [23]. However, the magnitudes of driving forces (e.g., recoil pressure, Marangoni force) under the relative low energy input (power of 36 W) and small melt pool size (depth of 2.1 μm) in laser polishing are different from the ones in laser metal AM (power of 100 – 500 W, pool depth of 50 – 400 μm [24]). Despite these studies on adding nanoparticles to improve surface finish, the concept of using nanoparticles to control melt flow to solve the intrinsic surface wave induced surface fluctuation problem in keyhole mode melting has not been reported.

Here we performed in-situ x-ray imaging experiment and, for the first time, demonstrated the effects of nanoparticles on melt flow behavior at every location of the melt pool using Al6061 + TiC nanoparticles system during the laser metal AM process. Nanoparticles damped the melt flow and surface wave before it solidified, resulting in a significant reduction of surface roughness. Our in-depth in-situ x-ray imaging analysis and viscosity measurement enable us to identify that nanoparticle-induced increase of viscosity causes the fully damping of the surface wave by (1) increasing the internal fluid friction for more efficient wave amplitude reduction, (2) controlling the melt flow to increase the surface wave number, (3) controlling the melt flow to increase the wave damping time. Furthermore, we also quantified the relative contributions of increasing fluid friction, increasing wave number, and increasing damping time to wave damping, which account for 61%, 25%, and 14%, respectively. The concept of using nanoparticles to damp surface waves

was further demonstrated to solve the surface wave problem encountered in keyhole-mode laser polishing of rough surfaces.

2. Materials and Methods

2.1 Materials and sample preparation

Al6061 + TiC system was used as a model system for this study because of the wide application of Al6061 and the chemical stability of TiC in the aluminum melt with neglectable reaction [25,26]. The Al6061 powders with the size of 17-60 μm were purchased from Valimet Inc (Stockton, CA, USA). The Al6061 substrate was cut from the commercial Al6061 plate purchased from McMaster-Carr (Elmhurst, IL, USA). The Al6061+TiC powders were prepared by ball milling of the Al6061 powders and TiC nanoparticles (83 nm, SSnano, Houston, TX, USA). The Al6061+TiC substrate was cut from the as-printed Al6061+TiC samples, which were fabricated by laser powder bed fusion (LPBF) of the ball-milled Al6061+TiC powders. To study the effects of nanoparticle volume fraction on the melt flow, two Al6061+TiC samples with different volume fractions of TiC nanoparticles were prepared: Al6061+1.8vol.%TiC, Al6061+4.4vol.%TiC.

17-4 precipitation hardening (17-4PH) stainless steel and ZrO_2 nanoparticles were used to further confirm that the nanoparticle-induced damping of the surface wave can be applied to other materials. The 17-4PH powders with the size of 26-56 μm were purchased from EOS GmbH (Krailling, Germany). The 17-4PH+5vol.%ZrO_2 powders were prepared by ball milling of the 17-4PH powders and ZrO_2 nanoparticles (40 nm, USnano, Houston, TX, USA). The ball-milled 17-4PH+5vol.%ZrO_2 powders were cold-pressed into a disc with the diameter of 10 mm and thickness of 1 mm for laser melting experiment. For reference, we also prepared the 17-4PH disc with the same size as the 17-4PH+5vol.%ZrO_2 disc using as-received 17-4PH powders by cold pressing. The chemical compositions of Al6061 powders, Al6061 plate, and 17-4PH powders are shown in

Table 1.

Table 1: Chemical composition in mass percentage of feedstock materials

Element	Al	C	Cr	Cu	Fe	Mg	Mn	Nb	Ni	Si	Ti	Zn
Al6061 powder	Balance	-	0.1	0.27	0.09	0.86	<0.01	-	-	0.55	0.01	<0.01
Al6061 plate	Balance	-	0.2	0.28	0.4	0.96	0.12	-	-	0.69	0.02	0.01
17-4PH powder	-	0.01	15.8	3.9	Balance	-	0.05	0.3	4.1	0.02	-	-

2.2 High-speed high-resolution x-ray imaging

High-speed high-resolution x-ray imaging was performed at Beamline 32-ID-B, Advanced Photon Source, Argonne National Laboratory to study the effects of nanoparticles on the melt flow and surface wave dynamics. During the experiment, a focused laser beam with a wavelength of 1070 nm and beam size of 90 μm (D4σ) was used to perform the laser melting experiment. At the same time, the x-ray penetrated through the sample, and the transmitted signal carrying the information of melt flow and surface wave dynamics was captured and recorded by a detection system (exposure time of 1 μs). The frame rate is 100 kHz to capture the melt flow dynamics, and 50 kHz to capture the surface wave dynamics. More information for the experimental setup is detailed in reference [27].

For laser melting experiment, the scan speed is fixed at 0.4 m/s. Different laser powers were used to study the melt flow and surface wave behavior under different melting modes for different materials: (1) under conduction mode, the laser powers used for Al6061, Al6061+1.8vol.%TiC, Al6061+4.4vol.%TiC are 390 W, 312 W, 286 W, respectively; (2) under keyhole mode, the laser powers used for Al6061, Al6061+1.8vol.%TiC, Al6061+4.4vol.%TiC are 416 W, 364 W, 338 W, respectively. Different laser powers were used for different materials to offset the absorptivity increase caused by the nanoparticles and, thus, to generate similar laser energy input, melt pool volume and vapor depression depth. Melt pool volume and vapor depression depth control melt

pool inertia [28] and recoil pressure (see Appendix A for detailed discussion), which are two important variables for melt pool oscillation and surface wave generation. Similar melt pool volume and keyhole depth allow us to exclude the effects from melt pool inertia and recoil pressure difference, so that we can study the pure nanoparticle effects on the melt flow and surface wave.

For the x-ray imaging experiment tracing the melt flow velocity, tungsten microparticles (1 vol.%, diameter ≤ 10 μm, USnano, Houston, TX, USA) were embedded in the Al6061 powders and Al6061+TiC powders by the ball milling process, which allowed for the incorporation of tungsten particles into the melt pool as flow tracers during LPBF of the Al6061 and Al6061+TiC [29]. The effects of tungsten particles on the melt flow are neglectable, as discussed in Appendix B.

2.3 Image processing

To characterize the melt flow behavior, the contrast of raw x-ray images was adjusted using the ImageJ software so that the movement of tungsten tracers can be clearly identified. We then quantified the moving velocity of tungsten tracers by dividing their displacement by their moving time. The displacement is obtained based on the 2D coordinate change of the tungsten tracers from one frame to the next frame in the recorded x-ray image sequences using ImageJ software. The moving time is the time interval before two consecutive frames, which was calculated according to the frame rate of 100 kHz.

2.4 Height profile of the scan track

The height profile of the scan track was captured by the Keyence LJ-V7000 laser profiler (Keyence, Osaka, Japan). The resolutions of the x-axis and y-axis are 20 μm, and 1 μm, respectively. The height resolution is 100 nm.

2.5 Surface tension and viscosity measurement

To explain the nanoparticle-induced wave damping phenomenon during LPBF process, we conducted the surface tension and viscosity measurement for the Al6061 and Al6061+TiC based on the oscillating droplet method [30]. During the experiment, the sample (1.3×10^{-2} g) was first placed on an inert ring with the inner diameter of 2 mm and thickness of 0.5 mm. The ring was attached to a linear solenoid. A continuous-wave laser with the power of 150 W, laser beam diameter (D4σ) of around 250 μm was used to heat and melt the sample for 2 s. After the laser heating/melting was over, the linear solenoid was immediately triggered to accelerate the inert ring, causing the droplet to pass through the ring due to the inertia, thereby introducing the initial deformation on the droplet. The droplet oscillation after passing through the ring was captured by a high-speed visible light camera (FASTCAM Nova S12, Photron, Tokyo, Japan) at a frame rate of 10 kHz. The surface tension was determined by the oscillation frequency, as denoted by the following equation:

$$\sigma = \frac{3\pi m f^2}{8} \tag{1}$$

where σ is the surface tension, f is the frequency of the oscillation, m is the mass of the liquid droplet. The viscosity was determined by the damping speed of the amplitude during the droplet oscillation:

$$\mu = \frac{3m}{10\pi d_0 t}\ln\left(\frac{\zeta_0}{\zeta}\right) \tag{2}$$

where μ is the viscosity, t is the oscillation time, d_0 is the equilibrium diameter of the droplet, ζ_0 is the initial amplitude, ζ is the final amplitude after oscillating t time. The chamber was evacuated and refilled with Argon gas three times before the experiment.

2.6 High-speed visible light imaging of surface wave dynamics

A high-speed visible light camera (FASTCAM Nova S12, Photron, Tokyo, Japan) was used to capture the surface wave dynamics (from the top view) during laser melting experiment for 17-4PH and 17-4PH+5vol.%ZrO_2. A continuous-wave (CW) ytterbium fiber laser (IPG YLR-500-AC, IPG Photonics, USA) was used to perform the single-track laser melting experiment on the 17-4PH and 17-4PH+5vol.%ZrO_2 discs. The view angle of the camera is 15º away from the normal direction of the disc surface. Imaging was performed at 50 kHz frame rate with an exposure time of 5 µs. The resolution is 4 µm. SugarCUBE Ultra illumination system (White LED Light SugarCUBE Ultra, Ushio, Tokyo, Japan) was used to illuminate the disc during the experiment.

2.7 Pre-sintering and laser polishing experiment

A continuous-wave ytterbium fiber laser (IPG YLR-500-AC, IPG Photonics, Oxford, MA, USA) was used to perform the pre-sintering and laser polishing experiment. The powder layer thickness is 100 µm. The laser power for the pre-sintering is 250 W. The laser power for the laser polishing is 500 W. The scan speed is 0.2 m/s for both. The laser beam diameter (D4σ) is around 250 µm. The hatch spacing is 80 µm. Keyence VHX-5000 digital microscope (Keyence, Osaka, Japan) was used to capture the optical images and height profile of the pre-sintered and polished surface. The height profile was captured based on the focus variation principle [31].

2.8 Surface roughness analysis

The surface roughness analysis was performed based on the ISO 4287 and ISO 4288 standard. The cut-off is 0.8 mm. The evaluation length is 4 mm. Two different surface profile parameters were used: (1) Ra: arithmetical mean deviation of the assessed profile; (2) Rz: maximum height of the profile.

3. Results and Discussion

3.1 Effects of nanoparticle on melt flow in conduction-mode LPBF process

We first performed the in-situ high-speed synchrotron x-ray imaging experiment to study the effects of nanoparticles on the melt flow behavior during conduction-mode LPBF process. The melt flow behavior of Al6061 and Al6061+TiC was successfully captured by the tungsten tracers during the x-ray imaging experiment (Fig. 1a-c). To clearly reveal the melt flow at different locations, the melt pool was divided into multiple cubic cells (50 μm × 50 μm), and the melt flow velocity of each cell was quantified according to the average velocity of tungsten microparticles within that cell during the x-ray imaging experiment (Fig. 1d-f). The quantified results show that, after adding 1.8vol.% TiC, 4.4vol.% TiC nanoparticles, the average flow speed of the whole melt pool decreased by 39%, 73%, respectively (Fig. 1h). The melt flow below the melt pool surface started to stagnate after adding nanoparticles and almost fully stalled for the Al6061+4.4vol.%TiC (Fig. 1d-f). The flow area ratio (defined as the melt pool area with liquid flowing/total melt pool area, the melt pool area mentioned in this paper is the projected area observed in x-ray images) decreased from 90% for the Al6061 to 68%, 47% for the Al6061+1.8vol.%TiC, Al6061+4.4vol.%TiC, respectively (Fig. 1i). The general trend of the effects of nanoparticles on melt flow behavior in the conduction-mode LPBF process is summarized in Fig. 1g.

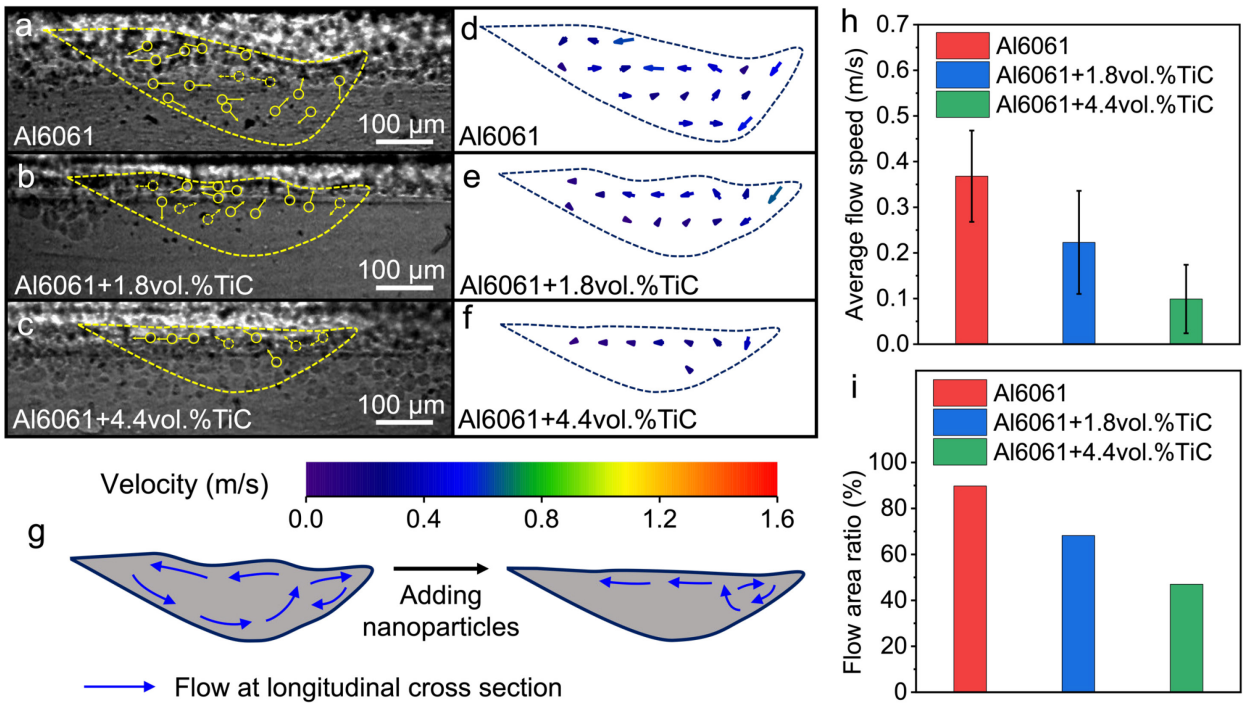

Fig. 1. Control of melt flow by nanoparticles in conduction-mode LPBF process. a-c*, X-ray images showing the instantaneous liquid flow direction during conduction-mode LPBF of Al6061, Al6061+1.8vol.%TiC, and Al6061+4.4vol.%TiC. The yellow solid circles indicate the W-tracers. The yellow solid arrows indicate the W-tracer trajectories. The yellow dashed circles and yellow dashed arrows represent the W-tracers and their moving trajectories obtained from other frames in the same experiment.* ***d-f****, Vector maps denoting the liquid flow velocity during LPBF.* ***g****, Schematic drawing indicating the effect of nanoparticles on melt flow in conduction-mode LPBF process.* ***h****, The average flow speed.* ***i****, The flow area ratio, which is defined as the ratio of the melt pool area with liquid flowing to the total melt pool area. The laser power for Al6061, Al6061+1.8vol.%TiC, Al6061+4.4vol.%TiC are 390 W, 312 W, 286 W, respectively. The laser power was selected to achieve a similar melt pool dimension. Adding nanoparticles decreases the laser power needed to achieve a similar melt pool dimension because TiC has higher absorptivity than Al6061 at 1070 nm wavelength* [26]*. The scan speed is 0.4 m/s for all. The laser beam diameter (D4σ) is 90 μm. The error bar indicates the standard deviation. The color scale for vector maps* ***d-f*** *is set to be consistent with that for Fig. 2****d-f*** *to compare the velocity difference between conduction mode and keyhole mode.*

3.2 Effect of nanoparticle on melt flow in keyhole-mode LPBF process

The effect of nanoparticles on melt flow in the keyhole-mode melting is rather complex, as revealed by x-ray images and quantified flow velocity during LPBF of the Al6061,

Al6061+1.8vol.%TiC, Al6061+4.4vol.%TiC (Fig. 2a-c). In the laser interaction domain, due to the continuous forward movement of the vapor depression, the liquid in front of the vapor depression needs to flow backward either through the liquid channels around the sides of vapor depression or beneath the vapor depression. After adding nanoparticles, we observed the liquid prefers to flow via the side of vapor depression instead of the bottom. Accordingly, the downwards flow speed ahead of vapor depression decreased from 1 m/s for Al6061 to 0.6 m/s for Al6061+1.8vol.%TiC and 0.4 m/s for Al6061+4.4vol.%TiC (Fig. 2h).

At the melt pool main body region (behind the vapor depression), we first observe the average flow speed decreased by 61%, 80% for the Al6061+1.8vol.%TiC, Al6061+4.4vol.%TiC, respectively, after adding nanoparticles (Fig. 2d-f, i). The thermocapillary flow covered almost the entire melt pool surface for Al6061. After adding nanoparticles, the thermocapillary flow stagnated before reaching the melt pool tail. The stagnation position is getting closer to the vapor depression as the volume fraction of nanoparticles increases (Fig. 2d-f). For Al6061, a clear vortex below the melt pool surface was observed, with a flow area ratio of 93%. After adding nanoparticles, the vortex disappeared. The flow area ratio plunged to 37% for the Al6061+1.8vol.%TiC, and further decreased to 24% for the Al6061+4.4vol.%TiC (Fig. 2j). The general trend of the effects of nanoparticles on melt flow behavior in the keyhole-mode LPBF process is summarized in Fig. 2g.

To explain the nanoparticle-induced change/damping of the melt flow behavior, we measured viscosity of Al6061, Al6061+1.8vol.%TiC, and Al6061+4.4vol.%TiC based on the oscillating droplet method. During the experiment, the free oscillation of the deformed droplets was clearly captured by the high-speed camera (Fig. 3a). The recorded high-speed images show that adding nanoparticles reduced the oscillating time required for the deformed droplet to return to the spherical shape due to the increase of viscosity. Based on the oscillating curve (Fig. 3b), the

calculated viscosity of the Al6061+1.8vol.%TiC (25.9 mPa·s) is 4.3 times higher, while the calculated viscosity of the Al6061+4.4vol.%TiC (79.4 mPa·s) is 15.2 times higher than that of the Al6061 (4.9 mPa·s).

The downwards flow ahead of vapor depression is driven by the vertical (downwards) component of recoil pressure, which provides the shear force at the gas-liquid interface. Nanoparticles can impair this flow by increasing viscosity. Hence, more liquid needs to flow horizontally through the channels around the sides of vapor depression. The horizontal flow is driven by the horizontal component of recoil pressure, which squeezes the liquid ahead of vapor depression to the back during the forward movement of vapor depression. This explains why the liquid prefers to flow via the side of vapor depression instead of the bottom after adding nanoparticles (Fig. 2d-f).

In the melt pool main body region, the surface melt flow is driven by the Marangoni force which promotes fluid flow and viscous force which impedes fluid flow [32]. The Marangoni force mainly depends on the temperature gradient and surface tension coefficient [33]. The viscous stress depends on the viscosity and velocity gradient perpendicular to the melt pool surface. When the liquid moves from vapor depression to the melt pool tail region, the Marangoni force decreases while the viscous force increases because: (1) The temperature gradient near the vapor depression is higher than that far away from vapor depression [34]; (2) The viscosity of the liquid near the vapor depression is lower due to the higher liquid temperature. The decrease of Marangoni force and the increase of viscous force explain why the horizontal flow velocity at the melt pool surface first increases and then decreases for both Al6061 and Al6061+TiC (Fig. 2d-f).

After adding nanoparticles, the viscosity increases, leading to the increase of the viscous force and reduction of flow velocity for both conduction mode and keyhole mode. The decrease of the

flow velocity further causes the decrease of inertial pressure of the fluid [29], which is the major driving force of the vortex flow below the melt pool surface. As a result, the vortex disappears after adding nanoparticles.

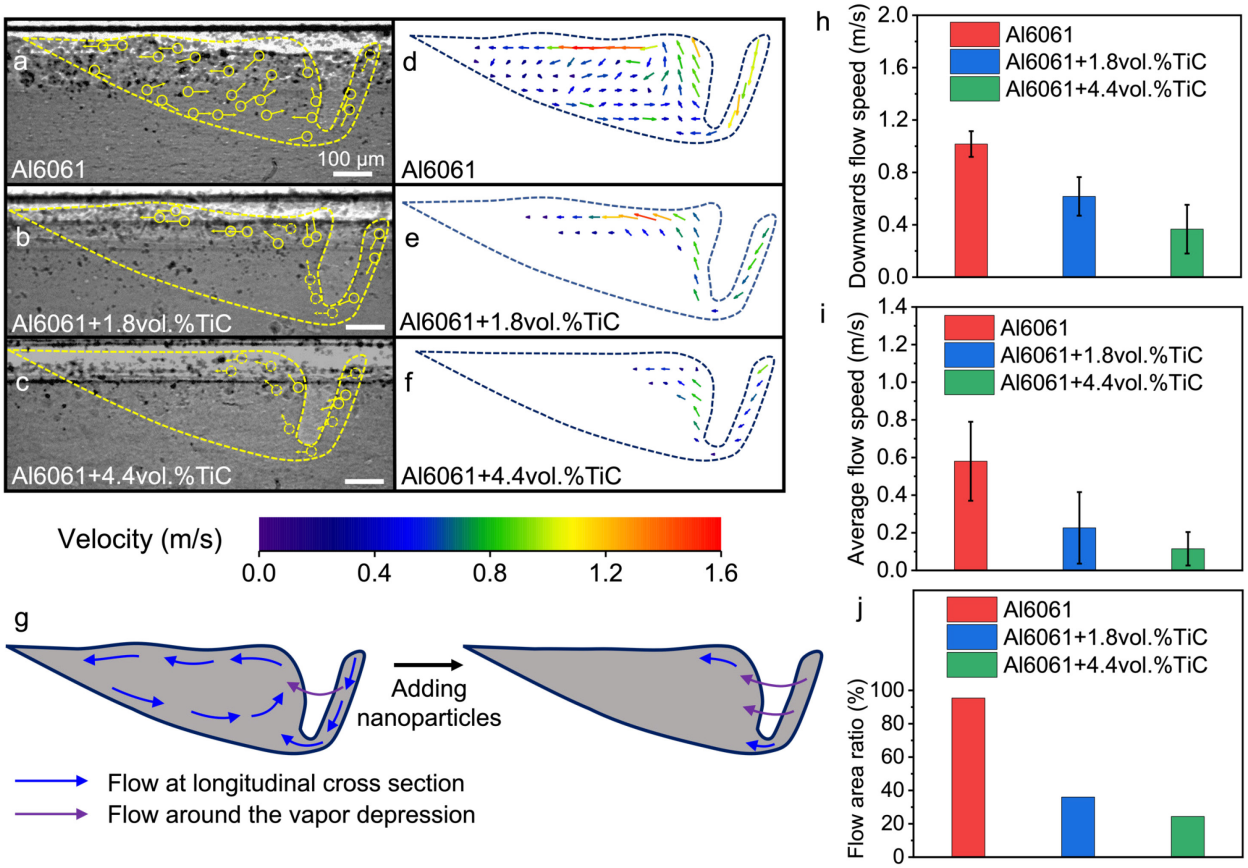

Fig. 2. Control of melt flow by nanoparticles in keyhole-mode LPBF process. a-c, *X-ray images showing the instantaneous liquid flow direction during keyhole-mode LPBF of Al6061, Al6061+1.8vol.%TiC, Al6061+4.4vol.%TiC. The yellow solid circles indicate the W-tracers. The yellow solid arrows indicate the W-tracer trajectories. The yellow dashed circles and yellow dashed arrows represent the W-tracers and their moving trajectories obtained from other frames in the same experiment.* ***d-f****, Vector maps denoting the liquid flow velocity.* ***g****, Schematic drawing indicating the effect of nanoparticle on melt flow during keyhole-mode LPBF process.* ***h****, The average speed of downwards flow ahead of vapor depression.* ***i****, The average flow speed of the whole melt pool.* ***j****, The flow area ratio. The laser power for Al6061, Al6061+1.8vol.%TiC, Al6061+4.4vol.%TiC are 416 W, 364 W, 338 W, respectively. The laser power was selected to achieve similar vapor depression and melt pool dimensions. Adding nanoparticles decreases the laser power needed to achieve a similar vapor depression dimension because TiC has higher absorptivity than Al6061 at 1070 nm wavelength. The scan speed is 0.4 m/s for all. The laser beam diameter (D4σ) is 90 μm. The error bar indicates the standard deviation.*

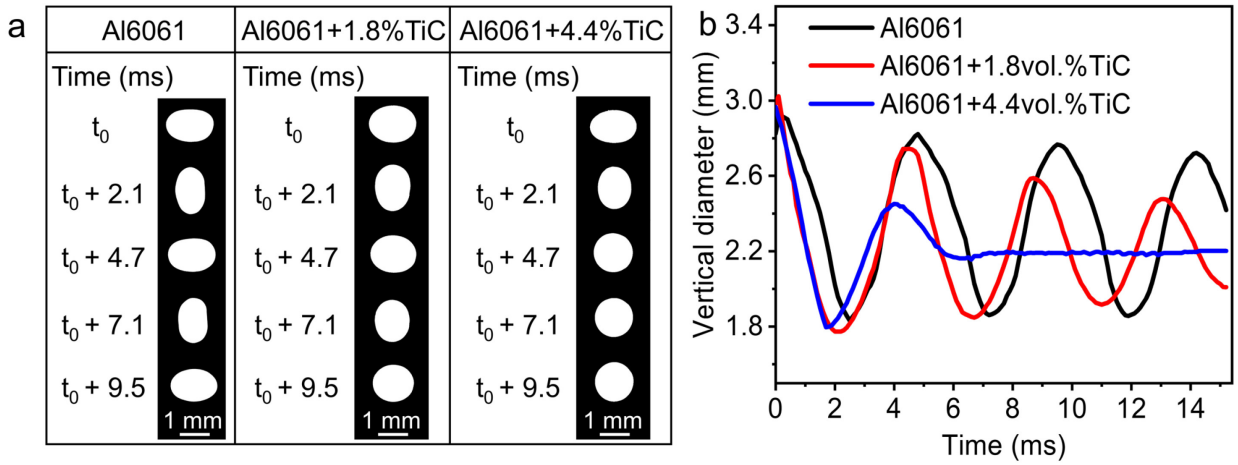

Fig. 3. The surface tension and viscosity measurement. ***a****, High-speed images showing the dynamic droplet morphology during oscillation.* ***b,*** *The droplet diameter as a function of time during oscillation.*

3.3 Damping of the surface wave by nanoparticles

We further studied the effects of nanoparticles on the surface wave dynamics during keyhole-mode melting by the in-situ x-ray imaging experiment (Fig. 4a-c). X-ray images clearly captured the surface wave that initiated at vapor depression rear wall, subsequently moved backward with the Marangoni flow, and finally was captured by solidification front. We quantified the amplitude of the surface waves as a function of the distance from the vapor depression rear wall. The results (Fig. 4d-e) show that the amplitude of the surface wave decreased during the backward movement due to the wave damping effect induced by viscous stress [35]. For the Al6061 and Al6061+1.8vol.%TiC, the amplitudes of surface waves captured by solidification front were 24.2 ± 11.3 μm and 12.4 ± 5.5 μm, respectively. In contrast, for the Al6061+4.4vol.%TiC, the surface waves were fully damped (not detectable by the x-ray imaging facility we used) before being captured by the solidification front (Fig. 4d-e, Supplementary Movie 1). The detailed discussion of surface wave formation mechanism is shown in Appendix C.

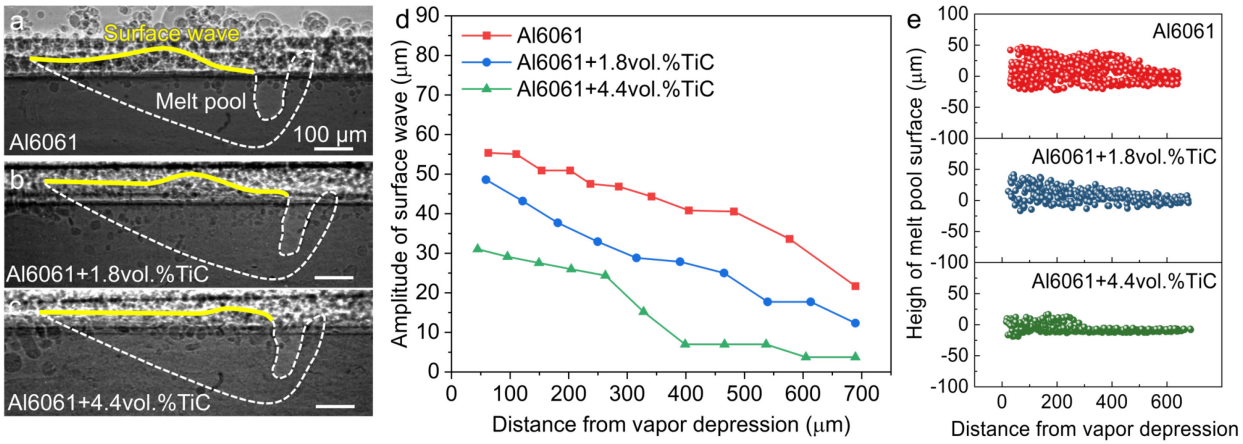

Fig. 4. Nanoparticle-induced damping of the surface wave during LPBF process. a-c*, x-ray images showing the surface wave during LPBF of Al6061, Al6061+1.8vol.%TiC, Al6061+4.4vol.%TiC, respectively.* ***d****, Surface wave amplitude as a function of the distance from vapor depression.* ***e****, Height of the melt pool surface as a function of the distance from vapor depression. The height of the melt pool surface in* ***e*** *is collected from multiple frames for each material. The laser power for Al6061, Al6061+1.8vol.%TiC, Al6061+4.4vol.%TiC are 416 W, 364 W, 338 W, respectively. The laser power was selected to achieve similar vapor depression and melt pool dimensions. The scan speed is 0.4 m/s for all. The laser beam diameter (D4σ) is 90 μm.*

3.4 Effects of nanoparticle-induced wave damping on surface finish

To study the effect of wave damping on surface finish, the height profile of the scan track was captured by a 3D profiler. The results (Fig. 5a-c) show that the track surface became smoother as the volume fraction of nanoparticles increased. Further analysis of surface roughness shows that compared with Al6061, the Ra of the Al6061+1.8vol.%TiC, Al6061+4.4vol.%TiC decreased by 30%, 68%, respectively (Fig. 5d). We extracted the height profile of the center line (parallel to laser scan direction) of the scan track. The periodic surface features induced by surface wave were clearly observed on the track surface of the Al6061 and Al6061+1.8vol.%TiC, but no clear periodic features exhibited on the Al6061+4.4vol.%TiC (Fig. 5e). This suggested that the damping of surface waves can significantly improve the surface finish.

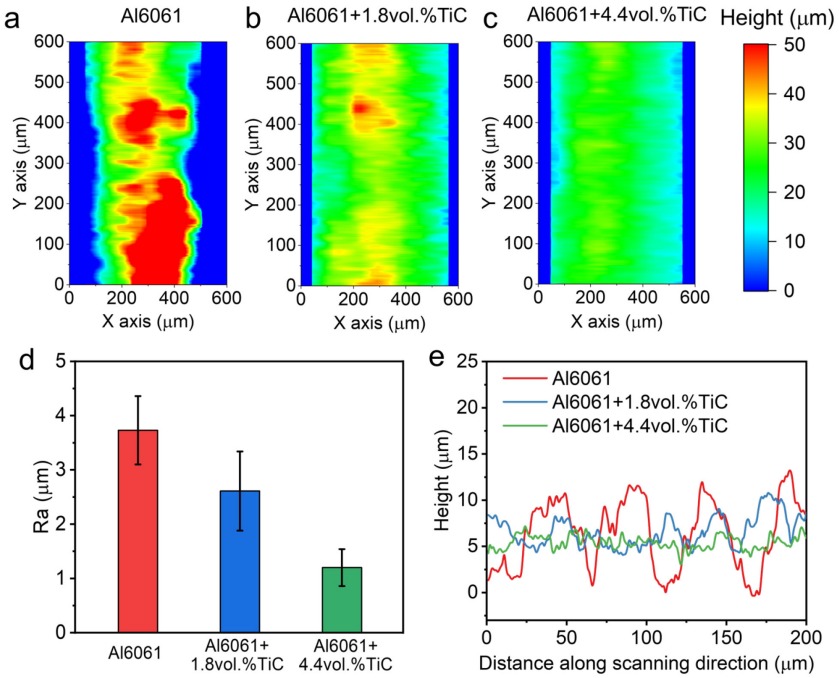

Fig. 5. Effect of nanoparticles on surface finish during LPBF process. a-c*, Track height profile of Al6061, Al6061+1.8vol.%TiC, Al6061+4.4vol.%TiC.* ***d****, The surface roughness (Ra) of the scan track. The error bar indicates the standard deviation.* ***e****, The built height of the centerline of the scan track.*

To prove that the periodic surface features on the printed surface were caused by the periodic surface waves, we quantified the spatial frequency of the surface asperity on the printed surface and the temporal frequency of the surface wave in the x-ray videos to verify that they have the following relationship:

$$f_t = v f_s \tag{3}$$

where f_t is the temporal frequency of the surface wave with the unit of s^{-1}, f_s is the spatial frequency of the surface asperity on the printed surface with the unit of m^{-1}, v is the scan speed with the unit of m/s.

To capture the temporal frequency of the surface wave, the liquid height fluctuation (relative change from the average value) at the vapor depression rear rim in the x-ray videos was quantified

and the peak in the liquid height versus time curve was identified as one surface wave (Fig. 6a-c). The temporal frequency of the surface wave was calculated by the following equation:

$$f_t = 1/T \quad (4)$$

where f_t is the temporal frequency, T is the average period of the surface waves (Fig. 6a-c). The calculated temporal frequencies of the Al6061, Al6061+1.8vol.%TiC and Al6061+4.4vol.%TiC are 7.4 kHz, 8.1 kHz, and 8.9 kHz, respectively.

The spatial frequency of the surface asperity on the printed surface was calculated based on the surface profile (Fig. 6d-e). The spatial frequency is the reciprocal of the surface asperity wavelength (i.e., the distance between two nearest humps) on the printed surface, as denoted by the equation below:

$$f_s = 1/D \quad (5)$$

where D is the wavelength of the surface asperity. The calculated spatial frequencies of the Al6061 and Al6061+1.8vol.%TiC based on the surface profile are 2.1×10^4 m^{-1}, 2.8×10^4 m^{-1}, respectively. There is no obvious periodic surface feature on the printed surface of Al6061+4.4vol.%TiC (Fig. 6f), due to the complete damping of the surface wave. For Al6061 and Al6061+1.8vol.%TiC, we observed that the spatial frequency of the surface asperity on the printed surface and the temporal frequency of the surface wave approximately follow the relationship in Equation (3). The difference of left side and the right side of Equation (3) for Al6061 is 12%, while that for Al6061+1.8vol.%TiC is 28%. This suggests that most of the surface asperities on the printed surface for the Al6061 and Al6061+1.8vol.%TiC were caused by the periodic surface waves. The slight deviation may be attributed to the additional surface asperities induced by the stochastic surface wave (See Appendix D).

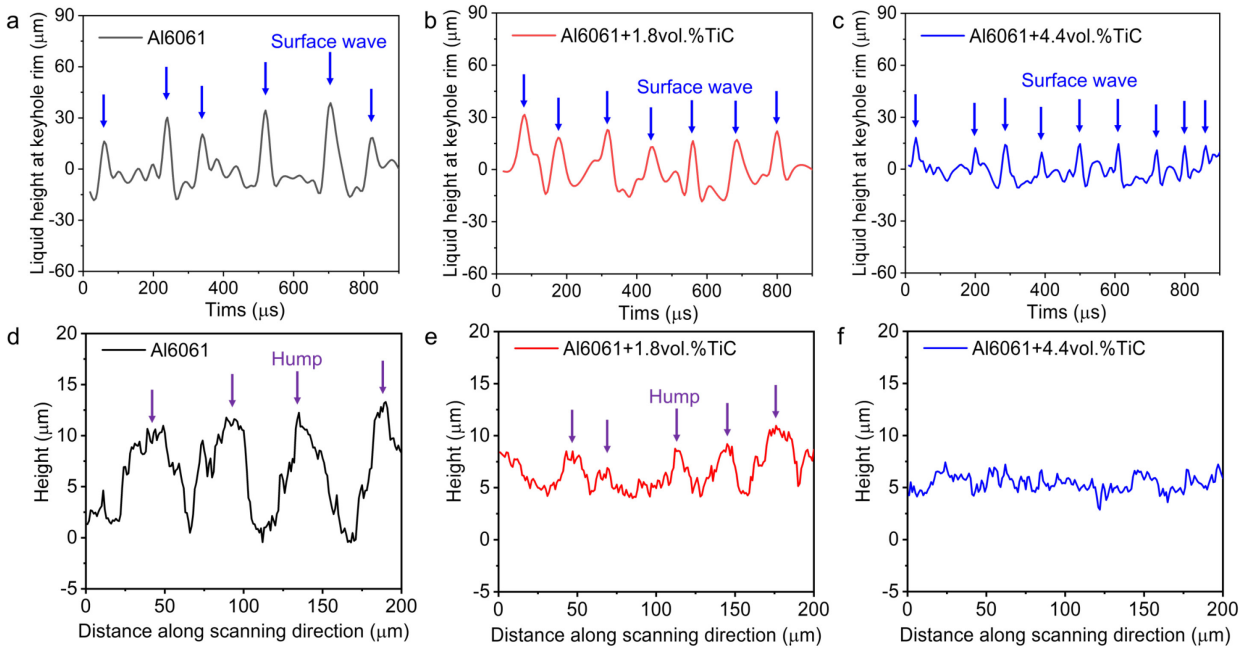

382

383 ***Fig. 6. Surface wave frequency. a-c,*** *The liquid height fluctuation at vapor depression rear rim*
384 *during LPBF of the Al6061 (**a**), Al6061+1.8vol.%TiC (**b**), and Al6061+4.4vol.%TiC (**c**). The peak*
385 *in the curve represents the generation of the surface wave.* ***d-f,*** *The surface height profile of the*
386 *scan track of Al6061 (**d**), Al6061+1.8vol.%TiC (**e**) and Al6061+4.4vol.%TiC (**f**) processed by*
387 *LPBF process.*
388

389 **3.5 Mechanism of nanoparticle-enabled damping of surface wave**

390 To explain the observed wave damping phenomenon, we performed in-depth in-situ x-ray
391 imaging analysis, which enables us to quantitively understand the mechanisms of nanoparticle-
392 induced damping of the surface wave based on the wave damping model [36]:

393 $$\zeta(t) = \zeta(0)\exp\left(-\frac{8\pi^2\mu k^2 t}{\rho}\right) \quad (6)$$

394 where $\zeta(t)$ is the final amplitude with the unit of m, $\zeta(0)$ is the initial amplitude with the unit of m,
395 t is damping time with the unit of s, μ is the dynamic viscosity with unit of Pa·s, k is the wave
396 number with the unit of m^{-1}, ρ is the density with the unit of kg/m^3. Based on Equation (6), the
397 increase of viscosity, or wave number, or damping time leads to a stronger damping effect. To

realize the effects of nanoparticles on the surface wave damping, we measured the viscosity and calculated the wave number and damping time of the Al6061 and Al6061+TiC. The results (Fig. 7a-d) show that the viscosity, surface wave number, and damping time all increased after adding TiC nanoparticles.

The measured viscosity of the Al6061+1.8vol.%TiC (25.9 mPa·s) is 4.3 times higher, while the measured viscosity of the Al6061+4.4vol.%TiC (79.4 mPa·s) is 15.2 times higher than that of the Al6061 (4.9 mPa·s), as detailed in Section 3.2. The viscosity enhancement causes the increase of the internal fluid friction during wave damping so that the wave amplitude will be reduced more efficiently [36].

The wave number and damping time were calculated based on the x-ray imaging data. The wave number is defined as the number of waves per unit distance at melt pool surface, which is related to the wave generation frequency and relative moving speed between vapor depression (moving forwards, speed equal to laser scanning speed) and surface wave (moving backward), as denoted by the following equation:

$$k = \frac{f}{v_s + v_w} \tag{7}$$

where f is the surface wave generation frequency, v_s is laser scan speed (0.4 m/s), v_w is the surface wave moving speed. As mentioned earlier, the surface wave generation frequencies of the Al6061, Al6061+1.8vol.%TiC, and Al6061+4.4vol.%TiC were captured by x-ray images as 7.4 kHz, 8.1 kHz, 8.9 kHz, respectively (Fig. 6a-c). The frequency increase after adding nanoparticles could be attributed to the increase of surface tension [37,38]. Based on the oscillating frequency during the oscillating droplet experiment, as shown in Fig. 3b, the calculated surface tensions of Al6061, Al6061+1.8vol.%TiC, and Al6061+4.4vol.%TiC are 0.68 $N \cdot m^{-1}$, 0.76 $N \cdot m^{-1}$ and 0.81 $N \cdot m^{-1}$, respectively. The surface wave moving speed was captured by x-ray images (Fig. 7e). Note that

421 the surface wave moving speed is higher than the flowing speed of the uppermost layer of the melt
422 pool captured by W-tracers (Fig. 2d-f). This is because: (1) the surface wave moving speed is a
423 combination of melt flow speed and wave propagation speed; (2) there is a boundary layer on the
424 melt pool surface, which is a thin layer of fluid immediately adjacent to the melt pool surface
425 caused by the Marangoni shear stress [39]. Within this boundary layer, the horizontal flow speed
426 suddenly decreases from surface to inside. The calculated boundary layer thickness is less than
427 105 μm, as detailed in Appendix E, which is in the similar range of velocity quantification cell
428 size (50 μm) for W-tracers. Therefore, the flow speed of the uppermost layer of the melt pool
429 captured by W-tracers, which is the average speed of melt flow within 50 μm depth from the top
430 surface, is smaller than the top surface flow speed. Based on the frequency and relative velocity,
431 the wave number was calculated based on Equation (7). The results (Fig. 7c) show that the wave
432 number of the Al6061+1.8vol.%TiC (2.6×10^3 m^{-1}) is 23% higher, while the wave number of the
433 Al6061+4.4vol.%TiC (3.7×10^3 m^{-1}) is 75% higher than that of the Al6061 (2.1×10^3 m^{-1}).

434 The damping time is defined as the lifetime of the surface wave, which was calculated by
435 dividing the melt pool length from vapor depression rear wall to melt pool tail by the relative
436 velocity of surface wave and vapor depression, as denoted by the following equation:

437 $$t = \frac{L}{v_s + v_w} \tag{8}$$

438 where t is the damping time, L is the length from vapor depression rear wall to melt pool tail, which
439 was captured by x-ray images. The calculated damping time (Fig. 7d) of the Al6061+1.8vol.%TiC
440 (0.26 ms) is 15% longer, while the damping time of the Al6061+4.4vol.%TiC (0.35 ms) is 55%
441 higher than that of the Al6061 (0.23 ms).

442 After obtaining the viscosity, wave number and damping time for the Al6061,
443 Al6061+1.8vol.%TiC, and Al6061+4.4vol.%TiC, we input these numbers into Equation (6) to

444 predict the final amplitude of surface wave after damping. The results (Fig. 7f) show that the
445 surface wave amplitude for Al6061 decreased by 13.5%, while the one of Al6061+1.8vol.%TiC
446 decreased by 69% after damping. In contrast, the amplitude of Al6061+4.4vol.%TiC decreased by
447 over 99.9% after damping. This indicates that nanoparticles can significantly improve the wave
448 damping effect by increasing viscosity, wave number, and damping time. The prediction result
449 that the Al6061+4.4vol.%TiC can almost fully damp the surface wave is consistent with our x-ray
450 observation (Fig. 4d).

451 While the viscosity of the material can be measured, the wave number and damping time are
452 hard to be measured without in-situ observation of the melt flow. Therefore, most of the previous
453 studies did not consider the effects of wave number and damping time change on the damping of
454 surface wave. Here in our work, the simultaneous quantification of the viscosity, wave number
455 and damping time enable us, for the first time, to study the individual contribution of viscosity,
456 wave number, and damping time during the wave damping of Al6061+4.4vol.%TiC. To be specific,
457 we performed another three calculations of wave damping based on Equation (6). For each
458 calculation, we used one increased number (viscosity, or wave number, or damping time) from
459 Al6061+4.4vol.%TiC, while other numbers were from Al6061, i.e., we change one factor at a time.
460 The individual increase of viscosity, wave number, and damping time results in a wave amplitude
461 decrease of 90%, 36%, 20%, suggesting an individual contribution (maintaining the relative ratio
462 relation) of 61%, 25%, 14%, respectively (Fig. 7g).

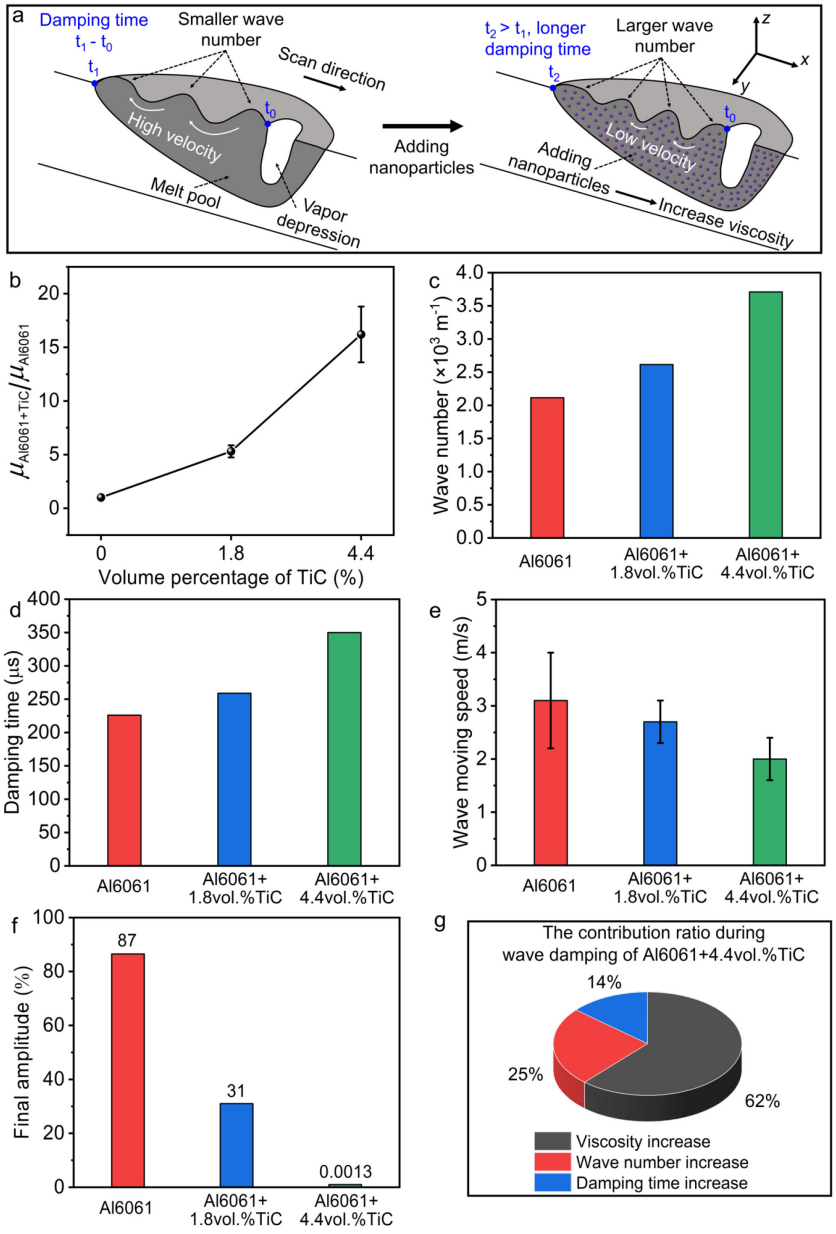

Fig. 7. The mechanism of nanoparticle-induced wave damping. ***a****, Schematic showing that nanoparticle damped surface wave by increasing the viscosity, wave number, and damping time.* ***b****, Viscosity of Al6061 and Al6061+TiC.* ***c-e****, The wave number* ***(c)****, and wave damping time* ***(d)****, wave moving speed* ***(e)*** *during LPBF of Al6061 and Al6061+TiC.* ***f****, The final wave amplitude of Al6061 and Al6061+TiC predicated by wave damping model.* ***g****, The contribution percentage of viscosity, wave number and damping time on wave damping. The error bar indicates the standard deviation.*

3.6 Nanoparticle-enabled damping of surface wave during laser melting of steel

To confirm the nanoparticle-enabled damping of surface wave is not just limited to aluminum alloy, we performed laser melting experiment for 17-4PH stainless steel and 17-4PH+5vol.%ZrO_2. The captured surface profile of the scan track shows that adding ZrO_2 nanoparticles significantly improved the surface finish (Fig. 8a, b). The surface finish improvement was attributed to the increase of the viscosity and damping of the surface wave by ZrO_2 nanoparticle, which was confirmed by the high-speed visible light imaging (See Supplementary Movie 2). Periodic surface features induced by the surface wave exhibited on the scan track of 17-4PH (Fig. 8c). In contrast, no obvious periodic surface feature was observed on the scan track of 17-4PH+5vol.%ZrO_2 (Fig. 8c). Further surface roughness analysis (Fig. 8d) shows that adding ZrO_2 nanoparticles results in a 63% decrease of Ra from 4.0 μm for 17-4PH to 1.5 μm for 17-4PH+5vol.%ZrO_2. This indicates that the concept of using nanoparticles to eliminate surface wave and improve the surface finish can be applied to other materials in fusion-based manufacturing process.

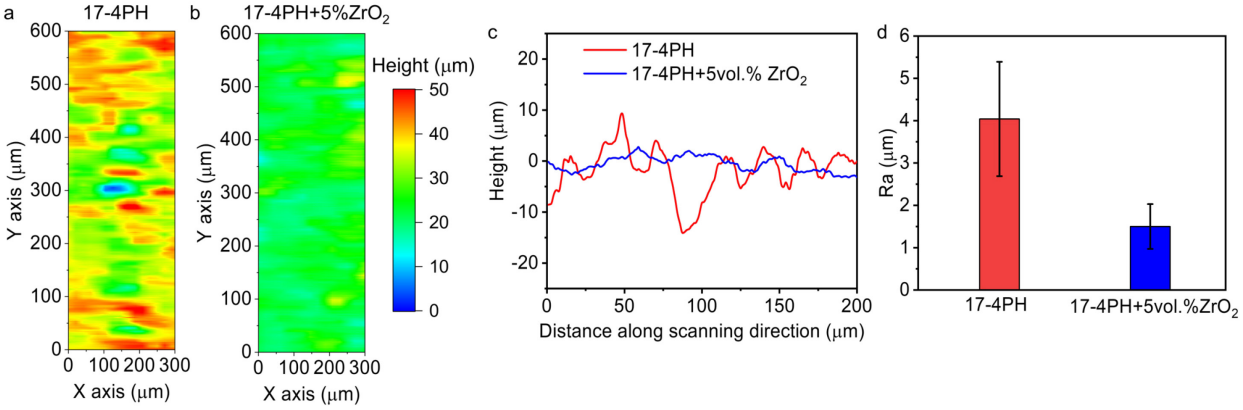

***Fig. 8. Nanoparticle-enabled damping of surface wave during laser melting of steel. a**, **b**, Track height profile of 17-4PH, and 17-4PH+5vol.%ZrO_2. **c**, The built height of the centerline of the scan track. **d**, The surface roughness (Ra) of the scan track. The error bar indicates the standard deviation.*

3.7 Wave-free keyhole-mode polishing of rough surface

We further demonstrate that our concept of using nanoparticle to damp the surface wave can also help to improve the laser polishing process. Laser polishing is a surface polishing process

using laser to melt the workpiece, resulting in the surface smoothing due to the surface tension and viscosity damping [40]. Previous research shows that keyhole-mode melting is required in laser polishing to polish the rough surface due to the larger pool dimension in keyhole-mode laser melting. However, keyhole-mode polishing introduces extra surface roughness induced by surface wave [41], limiting laser polishing application. Here we utilize nanoparticles to damp the surface wave, which enables us to achieve a wave-free keyhole-mode polishing of the rough surface. To demonstrate this, we created a rough surface by pre-sintering the powder bed (100 μm powder layer thickness) of Al6061 and Al6061+4.4vol.%TiC (Fig. 9a, e), and then polished the pre-sintered surface by keyhole-mode laser polishing (Fig. 9b, f). For both materials, the rough surface features induced by partially melt powders were smoothed after laser polishing. However, for the Al6061, we observed additional surface fluctuation induced by surface waves (Fig. 9b). In comparison, there were almost no noticeable wavy features for the Al6061+4.4vol.%TiC (Fig. 9f). The height profiles of pre-sintered surface and polished surface for Al6061 and Al6061+4.4vol.%TiC were captured by digital microscope based on the focus variation principle (Fig. 9c-d, g-h). Further surface roughness analysis shows that the Ra of the Al6061+4.4vol.%TiC decreased by 94% after polishing (from 45.7 μm to 2.9 μm), compared with a decrease of 35% (from 11.9 μm to 7.8 μm) for the Al6061. The Rz of the Al6061+4.4vol.%TiC decreased by 93% after polishing (from 217 μm to 16 μm) compared with a decrease of 50% (from 62 μm to 31 μm) for the Al6061.

Through the nanoparticle-enabled wave-free keyhole mode polishing, we can polish the rough surface with initial roughness far beyond these reported in previous laser polishing studies (Fig. 10), while still ensuring good polishing efficiency: 93% reduction of Ra. This is because we performed the laser polishing in keyhole mode, which significantly enhanced the melt pool

dimension. The expanded melt pool size enabled us to polish the large asperity on the melt pool surface. This explains why we can polish the extremely rough surface. At the same time, we introduced nanoparticles to solve the surface wave problem caused by the keyhole fluctuation in the keyhole mode polishing. Therefore, we can still achieve a relatively good polishing efficiency as compared with previous laser polishing works (Fig. 10).

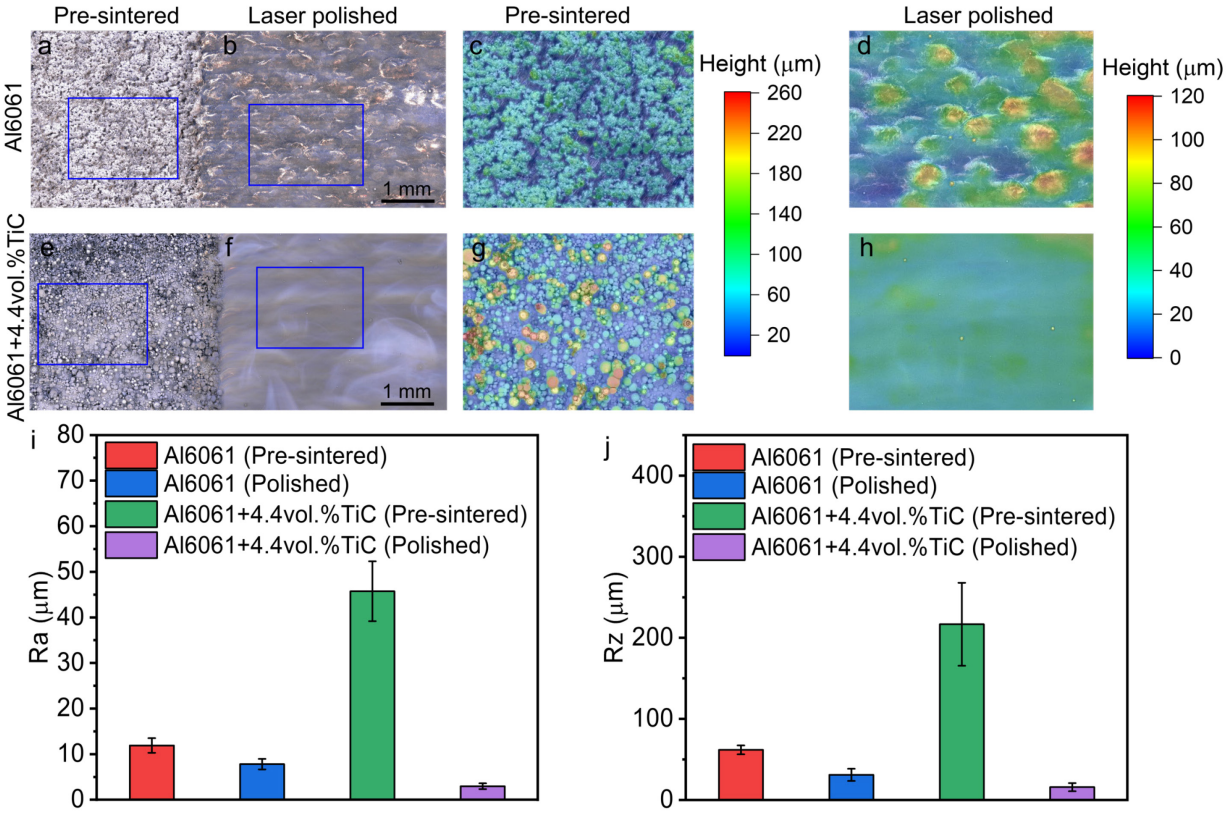

Fig. 9. Nanoparticle enabled wave-free keyhole-mode polishing of rough surfaces. a-b, *Optical images showing the pre-sintered* ***(a)*** *and polished surface* ***(b)*** *of Al6061.* ***c-d,*** *The height profile of pre-sintered* ***(c)*** *and polished surface* ***(d)*** *of Al6061.* ***e-f,*** *Optical images showing the pre-sintered* ***(e)*** *and polished surface* ***(f)*** *of Al6061+4.4vol.%TiC.* ***g-h,*** *The height profile of pre-sintered* ***(g)*** *and polished surface* ***(h)*** *of Al6061+4.4vol.%TiC.* ***c, d, g, h*** *were taken at the area indicated in* ***a, b, e, f,*** *respectively.* ***i-j****, The Ra* ***(i)*** *and Rz* ***(j)*** *of the pre-sintered and polished surface for Al6061 and Al6061+4.4vol.%TiC. The error bar indicates the standard deviation.*

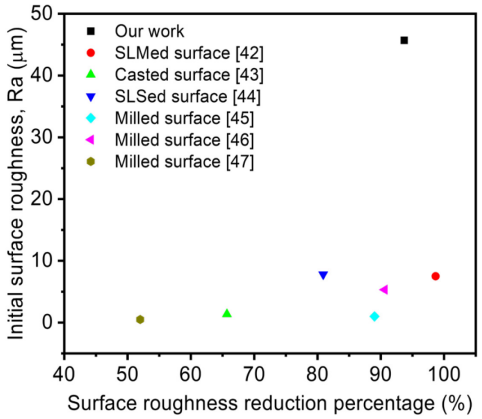

Fig. 10. The initial surface roughness and surface roughness reduction percentage reported in surface polishing research. *The data were collected from references* [42], [43], [44], [45], [46], [47].

4. Conclusion

In summary, we revealed the effects of nanoparticles on melt flow behavior at every location of melt pool during laser metal AM process and utilized nanoparticles to successfully control the melt flow and damp the surface wave, achieving significant surface finish improvement in the metal AM process and keyhole mode surface polishing. The main conclusions are as follows:

1. We experimentally revealed the effects of nanoparticles on the melt flow for the first time. Adding nanoparticle significantly reduced the melt flow speed in both conduction-mode and keyhole-mode LPBF process, resulting in the elimination of vortex.

2. After controlling melt flow by nanoparticles, the surface wave was fully damped before being captured by the solidification front. Therefore, the as-solidified surface finish was significantly improved after adding nanoparticles.

3. Our in-depth in-situ x-ray imaging analysis and viscosity measurement enable us to identify that nanoparticle-induced increase of viscosity causes the fully damping of the surface wave by (1) increasing the internal fluid friction for more efficient wave amplitude reduction, (2) controlling

the melt flow to increase the surface wave number, (3) controlling the melt flow to increase the wave damping time. Furthermore, we also quantified the relative contributions of increasing fluid friction, increasing wave number, and increasing damping time to wave damping, which account for 61.6%, 24.7%, and 13.7% respectively.

4. We further demonstrated that adding nanoparticle can achieve wave-free keyhole-mode polishing. Through the nanoparticle-enabled wave-free keyhole-mode polishing, we can polish the rough surface with initial roughness far beyond these reported in previous laser polishing, while still ensuring good polishing efficiency.

Our research provides the mechanisms and potential method to address the surface finish challenge in laser metal AM processes. Our concept of using nanoparticle to solve the intrinsic surface wave induced surface fluctuation problem can also improve the surface finish of intermediate layers during printing, which may significantly reduce the defects in the as-printed product. More work will be done in the future to gain deeper understanding of nanoparticle-enabled melt flow control and develop a feasible guideline for selecting/designing nanoparticles for different alloy systems to achieve desired melt flow and surface finish during laser metal AM.

Acknowledgements

This work is supported by US National Science Foundation and University of Wisconsin-Madison Startup Fund. This research used resources of the Advanced Photon Source, a U.S. Department of Energy (DOE) Office of Science User Facility operated for the DOE Office of Science by Argonne National Laboratory under Contract No. DE-AC02-06CH11357.

Appendix A: Comparing the melt flow and surface wave dynamics at similar vapor depression depth

We studied the effects of nanoparticle on the melt flow and surface wave dynamics under same vapor depression depth instead of same laser power because same vapor depression depth can rule out the effects from variation of laser energy input, recoil pressure, and melt pool dimension as much as possible to allow us to study the pure nanoparticle effects on melt flow and surface wave.

At 1070 nm wavelength, the absorptivity of TiC is 0.5 [48], which is higher than the absorptivity of 0.04 for Al6061 [49]. Therefore, adding TiC nanoparticles into Al6061 will increase the absorptivity. Hence, different laser powers should be used to create the condition with same or similar laser energy input. The laser energy input is directly related to the recoil pressure, which can be estimated by the following equation based on the pressure balance at the keyhole liquid interface [50]:

$$p_r = \rho_l g h + \frac{2\sigma}{R} \quad \text{(A.1)}$$

p_r is the vapor recoil pressure, ρ_l is the density of liquid, g is the gravity acceleration, h is the vapor depression depth, σ is the surface tension, R is the keyhole curvature, which can be estimated as laser beam radius.

If we performed the experiment at the same keyhole depth, the difference in the recoil pressure is only from surface tension difference. The surface tension value for Al6061 and Al6061+TiC is very close: compared with Al6061, the surface tension of Al6061+4.4vol.%TiC is 19% higher, while the surface tension of Al6061+1.8vol.%TiC is 12% higher, as detailed in Section 3.5. On the other hand, if we performed the experiment at the same laser processing parameter (e.g, 416 W, 0.4 m/s), the vapor depression depth significantly increased after adding nanoparticles:190 μm

for Al6061, 312 μm for Al6061+1.8vol.%TiC, 362 μm for Al6061+4.4vol.%TiC. This will add more variation in laser energy input and recoil pressure for different materials.

In addition, vapor depression depth determines the melt pool formation. Similar vapor depression depth usually guarantees a similar melt pool dimension. The melt pool dimension determines the total inertia of the liquid, which is critical variable controlling the melt flow, vapor depression/melt pool fluctuation and surface wave generation [28].

Based on above, we believe the comparison under same vapor depression depth is a relatively fair comparison to exclude the effects from variation of laser energy input, recoil pressure, and melt pool dimension. We also performed the experiment for Al6061 and Al6061+4.4vol.%TiC under the same laser processing parameter (416 W, 0.4 m/s). We observed the same phenomenon that adding nanoparticles can fully damp the surface wave and improve the surface finish.

Appendix B: Effects of tungsten particles on the melt flow

To trace the melt flow velocity during LPBF of Al6061 and Al6061+TiC, tungsten particles were added into the melt pool. Therefore, it is necessary to realize the effects of tungsten particles on the melt flow. Here we quantified the surface wave moving speed during LPBF of Al6061 and Al6061+1vol.%W by x-ray imaging (Fig. B.1). The results show that adding tungsten particles results in minor decrease of the surface wave moving speed from 3.1 ± 0.9 m/s to 3.0 ± 0.6 m/s. Hence, the effects of tungsten particles are neglectable compared with TiC nanoparticles, which decrease the surface wave moving speed to 2.0 ± 0.4 m/s. Moreover, the tungsten particles were added to both Al6061 and Al6061+TiC samples to trace the melt flow velocity. Therefore, the melt flow pattern difference during LPBF of Al6061 and Al6061+TiC indicated by tungsten tracers should be mostly caused by the added TiC nanoparticles instead of tungsten particles.

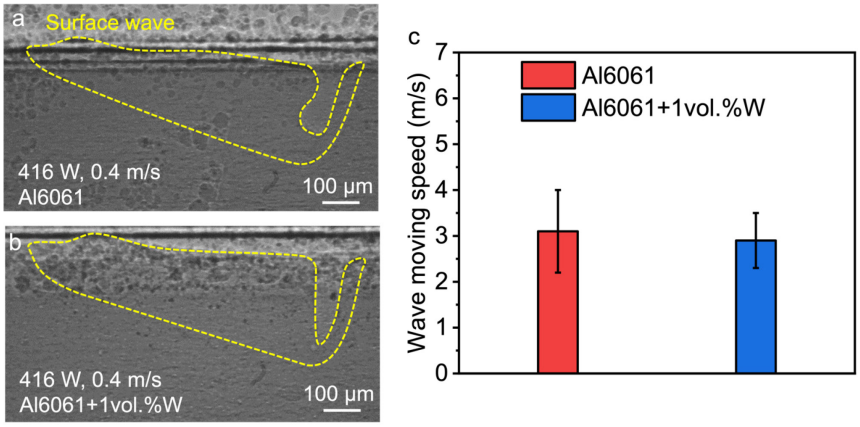

***Fig. B.1* Effects of tungsten particles on the melt flow.** a-b, X-ray images showing the surface wave during LPBF of Al6061 (a) and Al6061+4.4vol.%TiC (b). c, The surface wave moving speed.

Appendix C: Surface wave generation conditions and mechanisms

The surface waves were observed under both conduction mode and keyhole mode in our in-situ x-ray imaging experiment. However, the surface wave formation mechanisms are different for conduction mode and keyhole mode. Under conduction mode, the surface wave initiates at the laser-metal interaction position, which is probably due to the strong and unstable Marangoni flow at that area with extremely high temperature gradient (indicated by the white arrow in Fig. C.1a). Under keyhole mode, the surface wave is generated accompanied by the keyhole fluctuation. To be specific, when the keyhole suddenly expands, the liquid around the keyhole is squeezed out and the surface wave is generated at the keyhole rear rim (Fig. C.1b, c). Given that the amplitude of the surface wave under conduction mode is much smaller than that in keyhole mode and keyhole mode is widely adopted in laser metal AM [24], in the main text, we study the effects of nanoparticles on the surface wave behavior under keyhole mode.

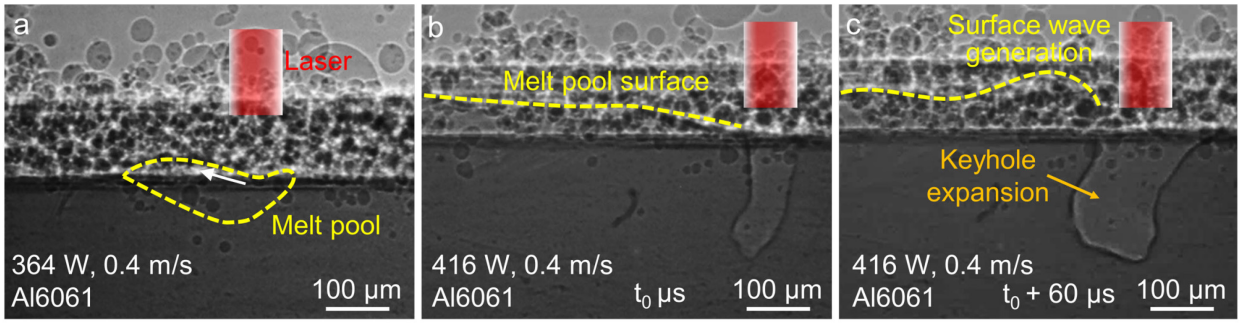

Fig. C.1 Surface wave formation mechanism. *a, X-ray image showing that the surface wave is induced by the strong and unstable Marangoni flow at the laser material interaction area under conduction mode. The Marangoni flow is indicated by the white arrow. b-c, X-ray images showing that the surface wave is induced by the keyhole expansion under keyhole mode.*

Appendix D: Nanoparticle-enabled damping of stochastic surface wave caused by the strong Marangoni flow

We have demonstrated that nanoparticles can damp the periodic surface wave originated from periodic oscillation of vapor depression. It was reported that the strong Marangoni flow can induce another type of stochastic surface wave at the melt pool tail region [51]. To be specific, when the strong Marangoni flow collides with the solidification front, it causes the rapid deceleration of fluid. According to Bernoulli's principle, the decrease of fluid speed increases the fluid static pressure and pushes the pool surface upward, resulting in the generation of stochastic surface wave at the melt pool end region. The amplitude of the surface fluctuation induced by the stochastic wave can be estimated as [52]:

$$a = (1 - K_{loss}) \left(\frac{\rho u^2 \omega^2}{\sigma} \right) \quad \text{(D.1)}$$

where a is the amplitude, K_{loss} is coefficient of energy loss induced by viscous dissipation and the collision between the surface flow and solidification front at the end of the melt pool, ρ is the fluid density, ω is the melt pool width, σ is the surface tension, u is the fluid speed before reaching the end of the melt pool, which is taken as flowing speed at melt pool surface 200 μm from the end of

the melt pool. Assuming K_{loss} is zero, which means that all the inertial pressure induced by flowing momentum is used to push the pool surface upward. The calculated amplitudes of Al6061, Al6061+1.8vol.%TiC, Al6061+4.4vol.%TiC are 115 μm, 7.2 μm, and 0 μm, respectively. This suggests that nanoparticles can also damp the stochastic surface wave by slowing down the melt flow reaching the end of the melt pool. After damping both the periodic surface wave caused by the vapor depression fluctuation and stochastic surface wave caused by the strong Marangoni flow, the surface finish was significantly improved after adding nanoparticles.

Appendix E: Estimation of the boundary layer thickness at the melt pool surface

The liquid flow during laser metal AM is very similar to the liquid flow on a flat plate, where there is a boundary layer (sudden velocity change) at the liquid-plate interface due to the shear stress between the liquid and plate. Here in laser metal AM, the shear stress is induced by the Marangoni force at the melt pool surface. Therefore, the boundary layer thickness at the top pool surface can be simply estimated as [53]:

$$\delta = 5\sqrt{\frac{\mu x}{\rho U}} \tag{E.1}$$

where δ is the boundary layer thickness with the unit of m, μ is the dynamic viscosity with the unit of Pa·s, x is the distance from vapor depression rear wall with the unit of m, ρ is the liquid density (2415 kg/m), U is the relative velocity between the melt pool surface and melt pool main body with the unit of m/s, here the propagation speed of surface wave in Fig. 7e was used. The calculated boundary layer thickness of the Al6061 increases from 0 to 105 μm as it develops along the melt pool surface (Fig. E.1). The size of the velocity quantification cell is 50 μm, which is within the range of boundary layer thickness, suggesting that there is a sudden velocity change within the

678 cell. This explains why the surface wave moving speed is higher than the average flow speed of
679 the W-tracers in the uppermost quantification cells of the melt pool.
680

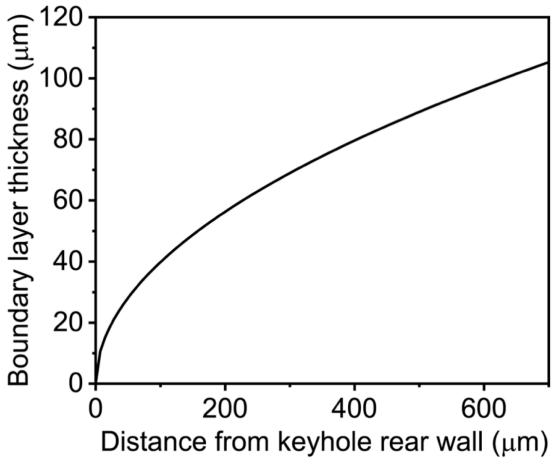

681

682 ***Fig. E.1. The boundary layer thickness at the melt pool surface as a function of the distance***
683 ***from vapor depression rear wall.***
684

685

686

687

688 **Reference**

689 [1] T. DebRoy, H.L. Wei, J.S. Zuback, T. Mukherjee, J.W. Elmer, J.O. Milewski, A.M.
690 Beese, A. Wilson-Heid, A. De, W. Zhang, Additive manufacturing of metallic
691 components – Process, structure and properties, Prog. Mater. Sci. 92 (2018) 112–224.
692 https://doi.org/10.1016/j.pmatsci.2017.10.001.
693 [2] T. DebRoy, T. Mukherjee, J.O. Milewski, J.W. Elmer, B. Ribic, J.J. Blecher, W. Zhang,
694 Scientific, technological and economic issues in metal printing and their solutions, Nat.
695 Mater. 18 (2019) 1026–1032. https://doi.org/10.1038/s41563-019-0408-2.
696 [3] Y.Y. Sun, S. Gulizia, C.H. Oh, D. Fraser, M. Leary, Y.F. Yang, M. Qian, The influence of
697 as-built surface conditions on mechanical properties of Ti-6Al-4V additively
698 manufactured by selective electron beam melting, JOM. 68 (2016) 791–798.
699 https://doi.org/10.1007/s11837-015-1768-y.
700 [4] H. Masuo, Y. Tanaka, S. Morokoshi, H. Yagura, T. Uchida, Y. Yamamoto, Y. Murakami,
701 Influence of defects, surface roughness and HIP on the fatigue strength of Ti-6Al-4V
702 manufactured by additive manufacturing, Int. J. Fatigue. 117 (2018) 163–179.
703 https://doi.org/10.1016/j.ijfatigue.2018.07.020.

[5] J. Gockel, L. Sheridan, B. Koerper, B. Whip, The influence of additive manufacturing processing parameters on surface roughness and fatigue life, Int. J. Fatigue. 124 (2019) 380–388. https://doi.org/10.1016/j.ijfatigue.2019.03.025.
[6] N. Senin, A. Thompson, R. Leach, Feature-based characterisation of signature topography in laser powder bed fusion of metals, Meas. Sci. Technol. 29 (2018) 045009. https://doi.org/10.1088/1361-6501/aa9e19.
[7] C. Tang, K.Q. Le, C.H. Wong, Physics of humping formation in laser powder bed fusion, Int. J. Heat Mass Transf. 149 (2020) 119172. https://doi.org/10.1016/j.ijheatmasstransfer.2019.119172.
[8] G. Strano, L. Hao, R.M. Everson, K.E. Evans, Surface roughness analysis, modelling and prediction in selective laser melting, J. Mater. Process. Tech. 213 (2013) 589–597. https://doi.org/10.1016/j.jmatprotec.2012.11.011.
[9] L. Caprio, A.G. Demir, B. Previtali, Observing molten pool surface oscillations during keyhole processing in laser powder bed fusion as a novel method to estimate the penetration depth, Addit. Manuf. 36 (2020) 101470. https://doi.org/10.1016/j.addma.2020.101470.
[10] S. Pang, L. Chen, J. Zhou, Y. Yin, T. Chen, A three-dimensional sharp interface model for self-consistent keyhole and weld pool dynamics in deep penetration laser welding, J. Phys. D. Appl. Phys. 44 (2011) 025301. https://doi.org/10.1088/0022-3727/44/2/025301.
[11] G. Pyka, A. Burakowski, G. Kerckhofs, M. Moesen, S. Van Bael, J. Schrooten, M. Wevers, Surface modification of Ti6Al4V open porous structures produced by additive manufacturing, Adv. Eng. Mater. 14 (2012) 363–370. https://doi.org/10.1002/adem.201100344.
[12] C. Bouland, V. Urlea, K. Beaubier, M. Samoilenko, V. Brailovski, Abrasive flow machining of laser powder bed-fused parts: Numerical modeling and experimental validation, J. Mater. Process. Technol. 273 (2019) 116262. https://doi.org/10.1016/j.jmatprotec.2019.116262.
[13] A.P. Nagalingam, H.K. Yuvaraj, S.H. Yeo, Synergistic effects in hydrodynamic cavitation abrasive finishing for internal surface-finish enhancement of additive-manufactured components, Addit. Manuf. 33 (2020) 101110. https://doi.org/10.1016/j.addma.2020.101110.
[14] P.J. DePond, G. Guss, S. Ly, N.P. Calta, D. Deane, S. Khairallah, M.J. Matthews, In situ measurements of layer roughness during laser powder bed fusion additive manufacturing using low coherence scanning interferometry, Mater. Des. 154 (2018) 347–359. https://doi.org/10.1016/j.matdes.2018.05.050.
[15] D. Gu, P. Yuan, Thermal evolution behavior and fluid dynamics during laser additive manufacturing of Al-based nanocomposites: Underlying role of reinforcement weight fraction, J. Appl. Phys. 118 (2015) 233109. https://doi.org/10.1063/1.4937905.
[16] C. Ma, L. Chen, C. Cao, X. Li, Nanoparticle-induced unusual melting and solidification behaviours of metals, Nat. Commun. 8 (2017) 14178. https://doi.org/10.1038/ncomms14178.
[17] C. Meng, F.G. Lu, H.C. Cui, X.H. Tang, Research on formation and stability of keyhole in stationary laser welding on aluminum MMCs reinforced with particles, Int. J. Adv. Manuf. Technol. 67 (2013) 2917–2925. https://doi.org/10.1007/s00170-012-4704-0.
[18] B. Almangour, D. Grzesiak, J.M. Yang, Rapid fabrication of bulk-form TiB2/316L stainless steel nanocomposites with novel reinforcement architecture and improved

performance by selective laser melting, J. Alloys Compd. 680 (2016) 480–493. https://doi.org/10.1016/j.jallcom.2016.04.156.
[19] M. Qu, Q. Guo, L.I. Escano, A. Nabaa, S.M.H. Hojjatzadeh, Z.A. Young, L. Chen, Controlling process instability for defect lean metal additive manufacturing, Nat. Commun. 13 (2022) 1079. https://doi.org/10.1038/s41467-022-28649-2.
[20] M. Qu, Q. Guo, L.I. Escano, S.J. Clark, K. Fezzaa, L. Chen, Mitigating keyhole pore formation by nanoparticles during laser powder bed fusion additive manufacturing, Addit. Manuf. Lett. 3 (2022) 100068. https://doi.org/10.1016/j.addlet.2022.100068.
[21] A. Simchi, H. Pohl, Direct laser sintering of iron-graphite powder mixture, Mater. Sci. Eng. A. 383 (2004) 191–200. https://doi.org/10.1016/j.msea.2004.05.070.
[22] A. Simchi, D. Godlinski, Effect of SiC particles on the laser sintering of Al-7Si-0.3Mg alloy, Scr. Mater. 59 (2008) 199–202. https://doi.org/10.1016/j.scriptamat.2008.03.007.
[23] C. Ma, L. Chen, J. Xu, J. Zhao, X. Li, Control of fluid dynamics by nanoparticles in laser melting, J. Appl. Phys. 117 (2015) 114901. https://doi.org/10.1063/1.4915276.
[24] R. Cunningham, C. Zhao, N. Parab, C. Kantzos, J. Pauza, K. Fezzaa, T. Sun, A.D. Rollett, Keyhole threshold and morphology in laser melting revealed by ultrahigh-speed x-ray imaging, Science. 363 (2019) 849–852. https://doi.org/10.1126/science.aav4687.
[25] A.E. Karantzalis, A. Lekatou, M. Georgatis, V. Poulas, H. Mavros, Casting-based production of Al-TiC-AlB2 composite material through the use of KBF4 salt, J. Mater. Eng. Perform. 20 (2011) 198–202. https://doi.org/10.1007/s11665-010-9668-3.
[26] T.C. Lin, C. Cao, M. Sokoluk, L. Jiang, X. Wang, J.M. Schoenung, E.J. Lavernia, X. Li, Aluminum with dispersed nanoparticles by laser additive manufacturing, Nat. Commun. 10 (2019) 4124. https://doi.org/10.1038/s41467-019-12047-2.
[27] Q. Guo, C. Zhao, L.I. Escano, Z. Young, L. Xiong, K. Fezzaa, W. Everhart, B. Brown, T. Sun, L. Chen, Transient dynamics of powder spattering in laser powder bed fusion additive manufacturing process revealed by in-situ high-speed high-energy x-ray imaging, Acta Mater. 151 (2018) 169–180. https://doi.org/10.1016/j.actamat.2018.03.036.
[28] S.A. Khairallah, T. Sun, B.J. Simonds, Onset of periodic oscillations as a precursor of a transition to pore-generating turbulence in laser melting, Addit. Manuf. Lett. 1 (2021) 100002. https://doi.org/10.1016/j.addlet.2021.100002.
[29] Q. Guo, C. Zhao, M. Qu, L. Xiong, S.M.H. Hojjatzadeh, L.I. Escano, N.D. Parab, K. Fezzaa, T. Sun, L. Chen, In-situ full-field mapping of melt flow dynamics in laser metal additive manufacturing, Addit. Manuf. 31 (2020) 100939. https://doi.org/10.1016/j.addma.2019.100939.
[30] C. Ma, J. Zhao, C. Cao, T. Lin, X. Li, Fundamental study on laser interactions with nanoparticles-reinforced metals—part II: effect of nanoparticles on surface tension, viscosity, and laser melting, J. Manuf. Sci. Eng. 138 (2016) 121002. https://doi.org/10.1115/1.4033446.
[31] L. Newton, N. Senin, C. Gomez, R. Danzl, F. Helmli, L. Blunt, R. Leach, Areal topography measurement of metal additive surfaces using focus variation microscopy, Addit. Manuf. 25 (2019) 365–389. https://doi.org/10.1016/j.addma.2018.11.013.
[32] C. Ma, M. Vadali, N.A. Duffie, F.E. Pfefferkorn, X. Li, Melt pool flow and surface evolution during pulsed laser micro polishing of Ti6Al4V, J. Manuf. Sci. Eng. Trans. ASME. 135 (2013) 061023. https://doi.org/10.1115/1.4025819.
[33] S.A. Khairallah, A.T. Anderson, A. Rubenchik, W.E. King, Laser powder-bed fusion additive manufacturing: Physics of complex melt flow and formation mechanisms of

pores, spatter, and denudation zones, Acta Mater. 108 (2016) 36–45. https://doi.org/10.1016/j.actamat.2016.02.014.
[34] S.M.H. Hojjatzadeh, N.D. Parab, W. Yan, Q. Guo, L. Xiong, C. Zhao, M. Qu, L.I. Escano, X. Xiao, K. Fezzaa, W. Everhart, T. Sun, L. Chen, Pore elimination mechanisms during 3D printing of metals, Nat. Commun. 10 (2019) 3088. https://doi.org/10.1038/s41467-019-10973-9.
[35] C. Ma, M. Vadali, X. Li, N.A. Duffie, F.E. Pfefferkorn, Analytical and experimental investigation of thermocapillary flow in pulsed laser micropolishing, J. Micro Nano-Manufacturing. 2 (2014) 021010. https://doi.org/10.1115/1.4027433.
[36] L.D. Landau, E.M. Lifshitz, Fluid mechanics, Pergamon Press, 1959.
[37] Y.H. Xiao, G. Den Ouden, Weld pool oscillation during GTA welding of mild steel, Weld. J. 72 (1993) 428–434.
[38] Y.H. Xiao, G. Den Ouden, A study of GTA weld pool oscillation, Weld. J. 69 (1990) 289–293.
[39] R.L. Akau, Thermocapillary flow in pulsed laser beam weld pools, Weld. J. 69 (1990) 23–29.
[40] A. Krishnan, F. Fang, Review on mechanism and process of surface polishing using lasers, Front. Mech. Eng. 14 (2019) 299–319. https://doi.org/10.1007/s11465-019-0535-0.
[41] B. Richter, N. Blanke, C. Werner, N.D. Parab, T. Sun, F. Vollertsen, F.E. Pfefferkorn, High-speed X-ray investigation of melt dynamics during continuous-wave laser remelting of selective laser melted Co-Cr alloy, CIRP Ann. 68 (2019) 229–232. https://doi.org/10.1016/j.cirp.2019.04.110.
[42] F. Zhihao, L. Libin, C. Longfei, G. Yingchun, Laser polishing of additive manufactured superalloy, Procedia CIRP. 71 (2018) 150–154. https://doi.org/10.1016/j.procir.2018.05.088.
[43] J. Schmidt, R. Scholz, H. Riegel, Laser polishing of aluminum by remelting with high energy pulses, Materwiss. Werksttech. 46 (2015) 686–691. https://doi.org/10.1002/mawe.201500318.
[44] A. Lamikiz, J.A. Sánchez, L.N. López de Lacalle, J.L. Arana, Laser polishing of parts built up by selective laser sintering, Int. J. Mach. Tools Manuf. 47 (2007) 2040–2050. https://doi.org/10.1016/j.ijmachtools.2007.01.013.
[45] J. Kumstel, B. Kirsch, Polishing titanium- and nickel-based alloys using cw-laser radiation, Phys. Procedia. 41 (2013) 362–371. https://doi.org/10.1016/j.phpro.2013.03.089.
[46] E. Ukar, A. Lamikiz, L.N. López de Lacalle, D. del Pozo, J.L. Arana, Laser polishing of tool steel with CO_2 laser and high-power diode laser, Int. J. Mach. Tools Manuf. 50 (2010) 115–125. https://doi.org/10.1016/j.ijmachtools.2009.09.003.
[47] A.M.K. Hafiz, E. V. Bordatchev, R.O. Tutunea-Fatan, Experimental analysis of applicability of a picosecond laser for micro-polishing of micromilled Inconel 718 superalloy, Int. J. Adv. Manuf. Technol. 70 (2014) 1963–1978. https://doi.org/10.1007/s00170-013-5408-9.
[48] B. Karlsson, J.E. Sundgren, B.O. Johansson, Optical constants and spectral selectivity of titanium carbonitrides, Thin Solid Films. 87 (1982) 181–187. https://doi.org/10.1016/0040-6090(82)90273-5.
[49] A.D. Rakić, Algorithm for the determination of intrinsic optical constants of metal films: application to aluminum, Appl. Opt. 34 (1995) 4755.

https://doi.org/10.1364/ao.34.004755.
[50] J. Kroos, U. Gratzke, G. Simon, Towards a self-consistent model of the keyhole in penetration laser beam welding, J. Phys. D. Appl. Phys. 26 (1993) 474–480. https://doi.org/10.1088/0022-3727/26/3/021.
[51] S. Kou, C. Limmaneevichitr, P.S. Wei, Oscillatory Marangoni flow: A fundamental study by conduction-mode laser spot welding, Weld. J. 90 (2011) 229–240.
[52] P.S. Wei, K.C. Chuang, J.S. Ku, T. Debroy, Mechanisms of spiking and humping in keyhole welding, IEEE Trans. Components, Packag. Manuf. Technol. 2 (2012) 383–394. https://doi.org/10.1109/TCPMT.2011.2178412.
[53] F.M. White, Fluid mechanics, 8th ed., McGraw-Hill Education, 2016.

CRediT author statement

Minglei Qu: Conceptualization, Formal analysis, Investigation, Methodology, Writing – original draft, Writing – review & editing. **Qilin Guo:** Investigation, Methodology, Validation. **Luis I. Escano:** Investigation. **Jiandong Yuan:** Investigation. **S. Mohammad H. Hojjatzadeh:** Investigation. **Samuel J. Clark:** Investigation. **Kamel Fezzaa:** Investigation. **Tao Sun:** Investigation. **Lianyi Chen:** Conceptualization, Supervision, Funding acquisition, Investigation, Methodology, Project administration, Resources, Writing – review & editing.